RSC Advances

PAPER

View Article Online
View Journal | View Issue

Cite this: *RSC Adv.*, 2022, **12**, 20138

A novel electrochemical sensor for glucose detection based on a $Ti_3C_2T_x$/ZIF-67 nanocomposite

Xuhui Han,[a] Ke Cao,†[c] Yanqing Yao,[a] Jia Zhao,[a] Chunpeng Chai *[a] and Pei Dai*[bc]

A $Ti_3C_2T_x$/ZIF-67 nanocomposite with outstanding conductivity has been prepared by loading ZIF-67 onto a two-dimensional $Ti_3C_2T_x$ nanosheet. $Ti_3C_2T_x$ sheets were synthesized by etching Ti_3AlC_2, and then ZIF-67 was grown *in situ* on the $Ti_3C_2T_x$ nanosheet. The $Ti_3C_2T_x$/ZIF-67 nanocomposite exhibits excellent detection performance for glucose, with a low LOD of 3.81 μM and wide linear detection range of 5–7500 μM. This terrific result is contributed by the synergistic effect of the high electrically conductive ability of $Ti_3C_2T_x$ and active catalytic performance of ZIF-67. Moreover, the electrochemical sensor prepared using the $Ti_3C_2T_x$/ZIF-67 nanocomposite also shows excellent selectivity, stability and repeatability for glucose detection. The $Ti_3C_2T_x$/ZIF-67 nanocomposite with outstanding performance has potential applications for electrochemical sensors.

Received 13th April 2022
Accepted 26th June 2022

DOI: 10.1039/d2ra02376h

rsc.li/rsc-advances

1. Introduction

Glucose is the direct energy source for human life activities. Many chronic diseases, such as diabetes, cardiovascular disease and other complications are closely related to blood glucose level.[1–5] Therefore, sensitive detection of glucose content in blood is of great value for monitoring human health. The advantage of an electrochemical method for detecting glucose compared to other methods is low cost, portability and high sensitivity.[6–8] The glucose sensors currently studied are mainly divided into enzyme-based glucose sensors and enzyme-free glucose sensors.[9–11] Although the traditional enzyme-based glucose sensor has good sensitivity and linearity, it needs to maintain the activity of the enzyme on the electrode surface, so its use and storage conditions are more stringent, which limits the development and application of glucose sensors to a certain extent.[12–14] In contrast, the enzyme-free sensor has the advantages of easy preparation, high sensitivity, and good stability, which has attracted the wide attention of researchers.[15–18] The development of highly active catalysts to promote electrocatalytic glucose oxidation is the key to non-enzymatic glucose sensing. So far, many precious metals, metal alloys and metal derivatives have been used to prepare non-enzymatic glucose sensors.[19–21]

Among them, metal–organic frameworks (MOFs) have attracted much attention due to their rich metal active sites, high porosity and electrochemical activity.[22–24] Based on these unique characteristics, MOFs have great potential in the fields of separation, energy storage, catalysis, *etc*.[25–27] It is worth noting that in recent years, MOFs have been used more as electrochemical sensing platform to detect certain substances, such as hydrazine,[6,28] dopamine,[29,30] hydrogen peroxide[31,32] and ascorbic acid. Generally, glucose electrochemical sensors related to MOF mainly focus on using MOF as an immobilized substrate or precursor of electrocatalyst.[33,35] For example, Ma *et al.* constructed an integrated dehydrogenase-based electrochemical sensor using zeolite imidazole frameworks (ZIFs) as substrate for glucose detection.[35] Shi *et al.* encapsulated Cu nanoparticles (NPs) on the ZIF-8 matrix for glucose sensing.[34] However, the poor electrical conductive ability of MOFs would greatly decrease the sensitivity of MOFs, which severely limits its application as an electrocatalyst for glucose detection in the electrocatalytic process.[36] Therefore, MOFs are usually composited with other conductive materials to overcome its shortcoming of poor conductivity.[37–40] MXene, a new type of two-dimensional nanomaterial, has attracted tremendous attention in recent years due to its large specific surface area, high hydrophilicity and intrinsic electrical conductivity.[41–43] These inherent conductivity of MXene makes it very suitable for improving the poor conductivity of MOF materials.

Based on the above discussion, the porous Co-based MOF (ZIF-67) was selected as the electrocatalyst for glucose detection and loaded on the two-dimensional MXene material ($Ti_3C_2T_x$) to prepare the $Ti_3C_2T_x$/ZIF-67 composite material. Then the

[a]*School of Materials Science and Engineering, Beijing Institute of Technology, Beijing 100081, China. E-mail: chaicp@bit.edu.cn*

[b]*State Key Laboratory of Chemical Resource Engineering, Beijing University of Chemical Technology, Beijing, 100029, China. E-mail: daipei008@126.com*

[c]*Beijing Key Laboratory of Radiation Advanced Materials, Beijing Research Center for Radiation Application Co.,Ltd., Beijing 100015, China*

† These authors contributed equally to this work and should be considered co-first authors.

obtained $Ti_3C_2T_x$/ZIF-67 composite was modified on glass–carbon electrode (GCE) to detect the electrochemical performance of glucose. $Ti_3C_2T_x$/ZIF-67 composite shows good electrochemical sensing performance for glucose, since $Ti_3C_2T_x$ makes up for the lack of conductivity of ZIF-67. This work provides an avenue to manufacture electrochemical sensors using MXene/MOFs composite materials.

2. Experimental section

2.1 Materials

Lithium fluoride (LiF, 98.5%), hydrochloric acid (HCl, 37%) were obtained from Sigma Aldrich. Ti_3AlC_2 powder (400 mesh) was purchased from 11 Technology Co., Ltd (JiLin, China). $Co(NO_3)_2 \cdot 6H_2O$, 2-methylimidazole, glucose and NaOH were bought from Fuchen Chemical Reagent Co., Ltd,. (Tianjin, China). All chemical reagents were analytical grade and used as received without further purification.

2.2 Preparation of MXene ($Ti_3C_2T_x$)

In the MXene ($Ti_3C_2T_x$) preparation process, LiF (1 g) was added into 20 mL HCl solation (9 mol L^{-1}) in a Teflon flask. After the LiF completely dissolved, Ti_3AlC_2 (1 g) powder was dispersed in the above mixture solution under magnetically stirring for 48 h at 35 °C. The resulting dispersion was washed with deionized water for a few times until pH ≈ 6, and the precipitate was collected and dried. Then multilayer $Ti_3C_2T_x$ (200 mg) was added into 100 mL deionized water under ultrasonic dispersion for 30 min. $Ti_3C_2T_x$ nanosheets were obtained after being centrifuged at 3500 rpm for 1 h.

2.3 Preparation of $Ti_3C_2T_x$/ZIF-67 composite

To prepare $Ti_3C_2T_x$/ZIF-67 composite, $Co(NO_3)_2 \cdot 6(H_2O)$ (1.455 g) was added in the mixed solution of methanol (40 mL)/ethanol (40 mL) under ultrasonication, and then 10 mL $Ti_3C_2T_x$ dispersion (5 mg mL^{-1}) was added under stirring for 0.5 h. And then 2-methylimidazole (1.642 g) was dispersed in another mixture of methanol (40 mL)/ethanol (40 mL) and directly added to the mixture solution, stirring magnetic force. After incubated for 24 h, the $Ti_3C_2T_x$/ZIF-67 was obtained by vacuum suction filtration, methanol washing and freeze-drying. For comparison, pure ZIF-67 without $Ti_3C_2T_x$ was also prepared by the same process.

2.4. Fabrication of the modified electrode

The glassy carbon electrode (GCE) was polish with alumina powder (0.3 μm and 0.05 μm). To prepare the modified GCE, $Ti_3C_2T_x$/ZIF-67 (10 mg) was added into ethanol (5 mL) under sonication for 30 min to obtain uniform dispersion. $Ti_3C_2T_x$/ZIF-67 suspension (10 μl) was pipetted and dropped onto GCE surface and drying at 25 °C. The other modified electrodes were prepared by the similar procedure.

2.5 Characterization

X-ray powder diffraction (XRD) spectra analyses the crystal structure of samples were carried out by the Bruker D8 with a Cu Kα radiation at a scan speed of 5°/min and a step size of 0.02°. The morphologies of the samples were observed by scanning electron microscopy (SEM, SU8020). X-ray photoelectron spectroscopy (XPS) analyses of the $Ti_3C_2T_x$/Cu-BTC nanocomposite were carried out by the Thermo ESCLAB 250 Xi (ThermoFisher Scientific, USA). All electrochemical properties were recorded by the IviumStat Electrochemical Workstation with a three electrodes system. In this system, glassy carbon electrode (GCE) was used as working electrode, Ag/AgCl and platinum flat were used as reference electrode and counter electrode respectively.

3. Results and discussion

3.1 Formation of $Ti_3C_2T_x$/ZIF-67 nanocomposite

According to the schematic diagram of the fabrication of the $Ti_3C_2T_x$/ZIF-67 nanocomposite (Scheme 1), the $Ti_3C_2T_x$/ZIF-67 was prepared by the $Ti_3C_2T_x$-templated growth of ZIF-67. The Co^{2+} ions were adhered to the surface of $Ti_3C_2T_x$ due to the electrostatic attraction of the oxygenic groups of $Ti_3C_2T_x$. The highly crystalline ZIF-67 was *in situ* grown on $Ti_3C_2T_x$ by the coordination reaction of Co^{2+} and N atom of 2-methylimidazole to form $Ti_3C_2T_x$/ZIF-67 nanocomposite.

3.2 Morphology of $Ti_3C_2T_x$/ZIF-67 nanocomposite

The morphology and microstructure of $Ti_3C_2T_x$/ZIF-67 nanocomposite were characterized by scanning electron microscope. The SEM image of the Ti_3AlC_2 particles was shown in Fig. 1(a), and it can be seen that the raw material Ti_3AlC_2 has a clear and compact layered three-dimensional structure. As shown in Fig. 1(b), Ti_3AlC_2 transformed into a well-resolved loosely stacked accordion-like structure after etching reaction. $Ti_3C_2T_x$ nanosheets (Fig. 1(c)) exhibited the single/few layered structure (f-$Ti_3C_2T_x$) by sonication treatment. The Fig. 1(d) was shown that ZIF-67 clearly presented the typical dodecahedron morphology with a uniform size ~250 nm. In order to prove the homogeneous particles on the surface of $Ti_3C_2T_x$ were ZIF-67 in Fig. 1(e) and (f), the EDS mapping was employed. The result confirmed that the elements (Ti, Co, N, C and O) were existed on the surface of $Ti_3C_2T_x$/ZIF-67 nanocomposite (Fig. 2). Among them, Ti was belonged to $Ti_3C_2T_x$, while N and Co was attributed to ZIF-67. The EDS mapping further verified the presence of $Ti_3C_2T_x$ and ZIF-67 in the composite, demonstrating that ZIF-

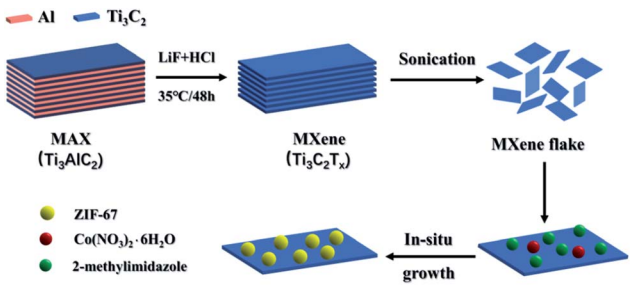

Scheme 1 Schematic diagram of the preparation of the $Ti_3C_2T_x$/ZIF-67 nanocomposite.

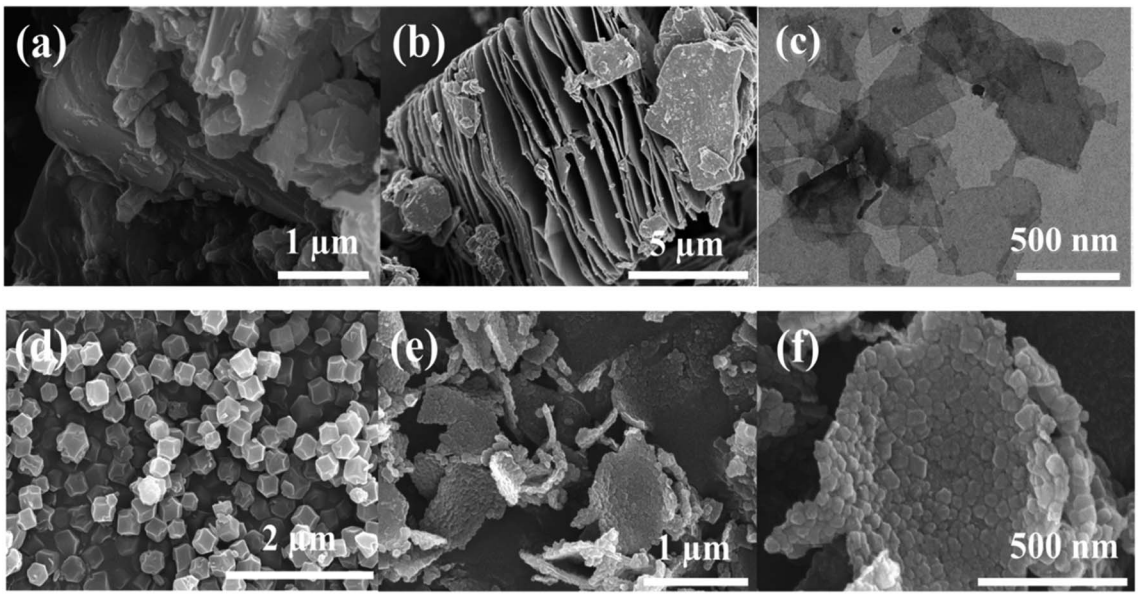

Fig. 1 SEM image of (a) Ti_3AlC_2, (b) $Ti_3C_2T_x$, (d) ZIF-67, (e) and (f) $Ti_3C_2T_x$/ZIF-67 with different magnifications. TEM image of (c) f-$Ti_3C_2T_x$ flake.

67 particles have been successfully distributed on the $Ti_3C_2T_x$ nanosheets.

3.3 Crystal structure of $Ti_3C_2T_x$/ZIF-67 nanocomposite

The crystal structure of Ti_3AlC_2, $Ti_3C_2T_x$, ZIF-67 and $Ti_3C_2T_x$/ZIF-67 nanocomposite was analyzed by the XRD spectra. The diffraction peaks at 9.58°, 19.2° and 39.04° in the XRD spectrum of Ti_3AlC_2 was corresponded to the (002), (004) and (104) planes of crystalline Ti_3AlC_2, respectively. Compared with Ti_3AlC_2, the characteristic peaks at 19.2° and 39.04° were not appeared and the diffraction peak (002) shifted to a smaller angle in the XRD pattern of $Ti_3C_2T_x$, which proved the effectiveness of the synthesis procedure. The characteristic diffraction peaks of the ZIF-67 were entirely consistent with the well-known structure of ZIF-67 crystal, which demonstrate that the synthesized ZIF-67 purity is high. The diffraction peaks of ZIF-67 could be well recognized in the XRD spectrum of $Ti_3C_2T_x$/ZIF-67 indicating that the presence of $Ti_3C_2T_x$ does not affect the growth of ZIF-67 crystals. All the rustles illustrated that ZIF-67 particles have grown on the $Ti_3C_2T_x$ nanosheets. The surface characteristic of $Ti_3C_2T_x$/ZIF-67 nanocomposite was analyzed by XPS (Fig. 3(b)). It can be seen that the six peaks of 285 eV, 399 eV, 455 eV, 531 eV, 685 eV and 811 eV of $Ti_3C_2T_x$/ZIF-67 correspond to the elements C 1s, N 1s, Ti 2p, O 1s, F 1s and Co 2p. Among them, Co 2p and N 1s are characteristic elements of ZIF-67, while Ti 2p and F 1s

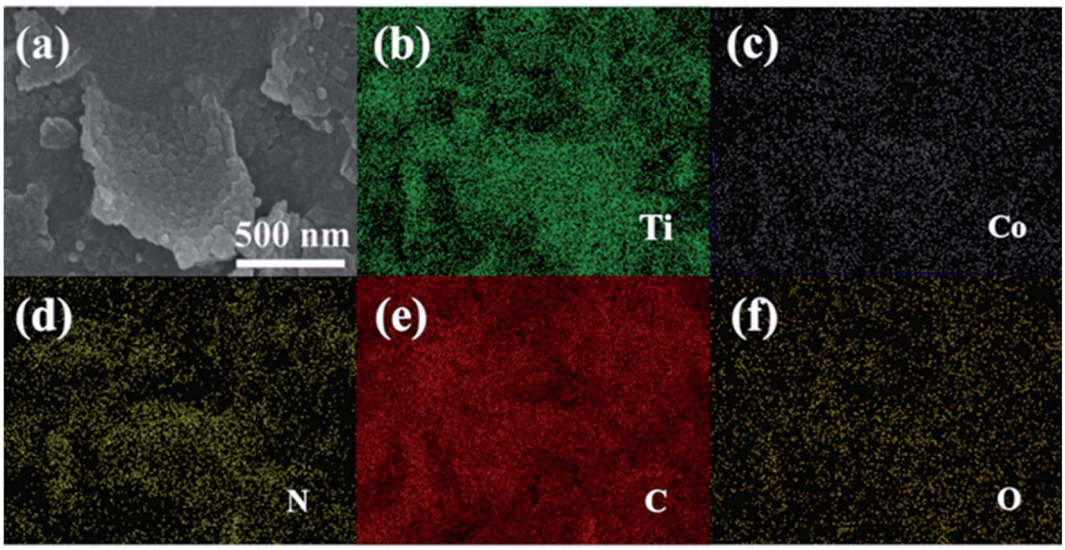

Fig. 2 The EDX mapping analysis of $Ti_3C_2T_x$/ZIF-67.

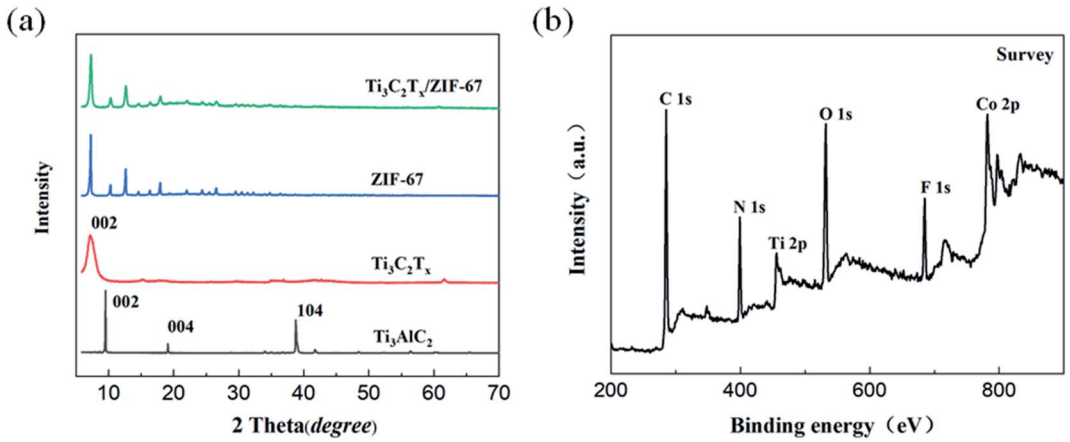

Fig. 3 (a) XRD patterns of Ti_3AlC_2, $Ti_3C_2T_x$, ZIF-67 and $Ti_3C_2T_x$/ZIF-67. (b) XPS survey scan of $Ti_3C_2T_x$/ZIF-67.

are derived from $Ti_3C_2T_x$, which further indicates the successful preparation of $Ti_3C_2T_x$/ZIF-67 nanocomposites.

3.4 Surface area and porosity of $Ti_3C_2T_x$/ZIF-67 nanocomposites

The surface area and porosity of ZIF-67 and $Ti_3C_2T_x$/ZIF-67 nanocomposites were measured by nitrogen adsorption/desorption experiments. Fig. 4(a) and (c) are the N_2 adsorption/desorption isotherms of ZIF-67 and $Ti_3C_2T_x$/ZIF-67, respectively. It can be seen that ZIF-67 and $Ti_3C_2T_x$/ZIF-67 both exhibit typical type I curve, suggesting that ZIF-67 and $Ti_3C_2T_x$/ZIF-67 are both microporous structures. Fig. 4(b) and (d) are the pore size distribution curves of ZIF-67 and $Ti_3C_2T_x$/ZIF-67, respectively. It can be seen that the pore size distribution is mainly concentrated at about 1.9 nm, mainly micropores, which is consistent with the corresponding adsorption/desorption isotherm. In addition, the specific surface area of ZIF-67 and $Ti_3C_2T_x$/ZIF-67 are 1546 $m^2\ g^{-1}$ and 678 $m^2\ g^{-1}$,

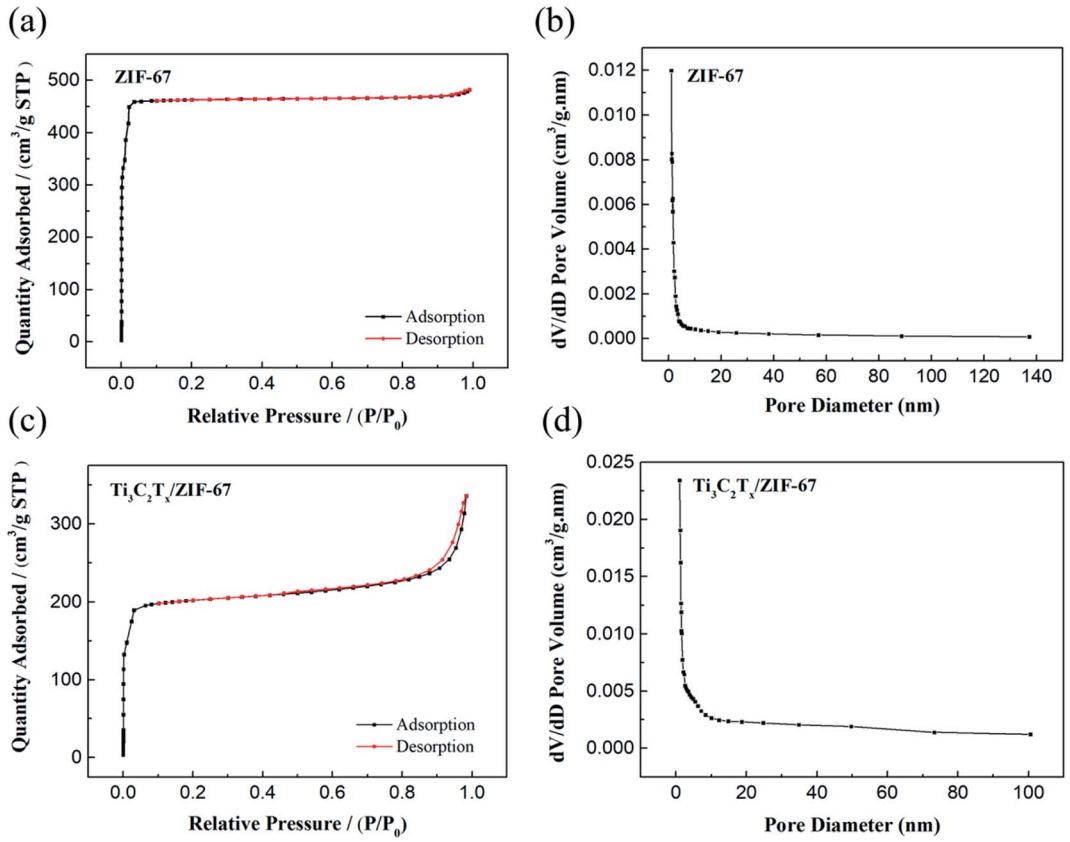

Fig. 4 N_2 adsorption/desorption isotherms of ZIF-67 (a) and $Ti_3C_2T_x$/ZIF-67 (c); pore size distribution curves of ZIF-67 (b) and $Ti_3C_2T_x$/ZIF-67 (d).

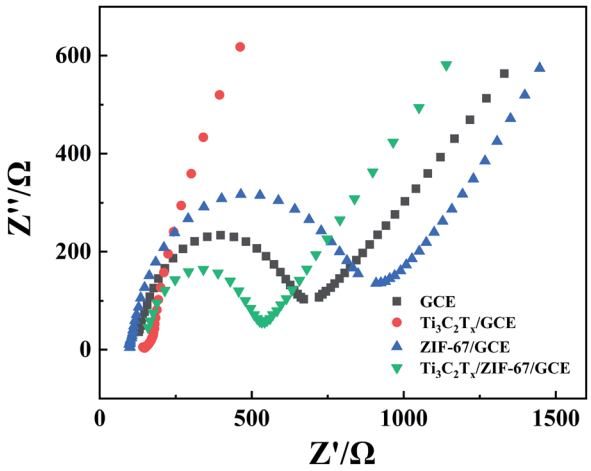

Fig. 5 Nyquist plots of EIS for GCE, $Ti_3C_2T_x$/GCE, ZIF-67/GCE and $Ti_3C_2T_x$/ZIF-67/GCE.

respectively. It means that the $Ti_3C_2T_x$/ZIF-67 specific surface area is smaller than that of ZIF-67. This is due to the $Ti_3C_2T_x$ nanosheets with dense film structure do not contribute much to the specific surface area.

3.5 Impedance analysis

The electrochemical property of $Ti_3C_2T_x$/ZIF-67 was studies by electrochemical impedance spectroscopy (EIS). In this research, EIS experiments was performed in 5 mM $[Fe(CN)_6]^{3-/4-}$ with 0.1 M KCl at 10 mV AC voltage in the frequency range of 0.1 Hz to 10 kHz. The EIS of these nanocomposites and bare GCE were shown in Fig. 5. The bare GCE EIS had a semicircular portion at higher frequencies. The semicircle diameter of EIS of ZIF-67/GCE has increased due to the inherent insulation of ZIF-67. However, the curve of $Ti_3C_2T_x$/GCE had no obvious semicircular part, even close to linear, which was related to the outstanding metal conductivity of $Ti_3C_2T_x$. The semicircle diameter of $Ti_3C_2T_x$/ZIF-67/GCE was between $Ti_3C_2T_x$/GCE and bare GCE, which suggested that its electron transfer rate was greatly improved compared to ZIF-67/GCE. The EIS result proved that The $Ti_3C_2T_x$ nanosheets were an important component to enhance the electrochemical conductivity of $Ti_3C_2T_x$/ZIF-67.

3.6 Electrocatalytic behaviors of the sensor

The electrocatalytic ability of $Ti_3C_2T_x$/ZIF-67 composite for glucose was studied by CV curve characterization analysis. The typical CV curves of GCE, ZIF-67/GCE and $Ti_3C_2T_x$/ZIF-67/GCE with or without 1 mM glucose in 0.1 M NaOH electrolyte were shown in Fig. 6(a). It can be seen that no obvious redox peaks were observed for bare GCE with or without glucose, which indicated that the bare GCE cannot catalyze glucose. Compared with the bare GCE, the redox peaks value of ZIF-67/GCE were nearby 0.30 V because of the conversion of Co(II) and Co(III). It was worth noting that the anodic peak current increased significantly after adding glucose. This provided that ZIF-67 has prominent catalytic activity for the oxidation of glucose. The reaction mechanism can be explained by eqn (1) and (2):

$$[Co(II)(min)_2]_n + nOH^- \rightarrow [Co(III)(min)_2(OH)]_n + ne^- \quad (1)$$

$$Co(III) + glucose \rightarrow Co(II) + gluconolactone \quad (2)$$

The oxidation process of glucose by $Ti_3C_2T_x$/ZIF-67 was displayed in Fig. 7. Co(II) was oxidized to Co(III) initially, and then to oxidize glucose molecules to gluconolactone through Co(III), and finally Co(III) was reduced to Co(II). For the $Ti_3C_2T_x$/ZIF-67/GCE, an obvious current response appeared with glucose added, which was owing to the presence of $Ti_3C_2T_x$ with high conductivity that provides a greater electron transfer rate. Meantime, the cyclic voltammograms of $Ti_3C_2T_x$/ZIF-67 at 10–500 mV s^{-1} were also tested. As shown in Fig. 6(b), the peak current increased accordingly with the scan rate increasing from 10 to 500 mV s^{-1}, and exhibited good linear, which indicated a diffusion-controlled electrochemical process.

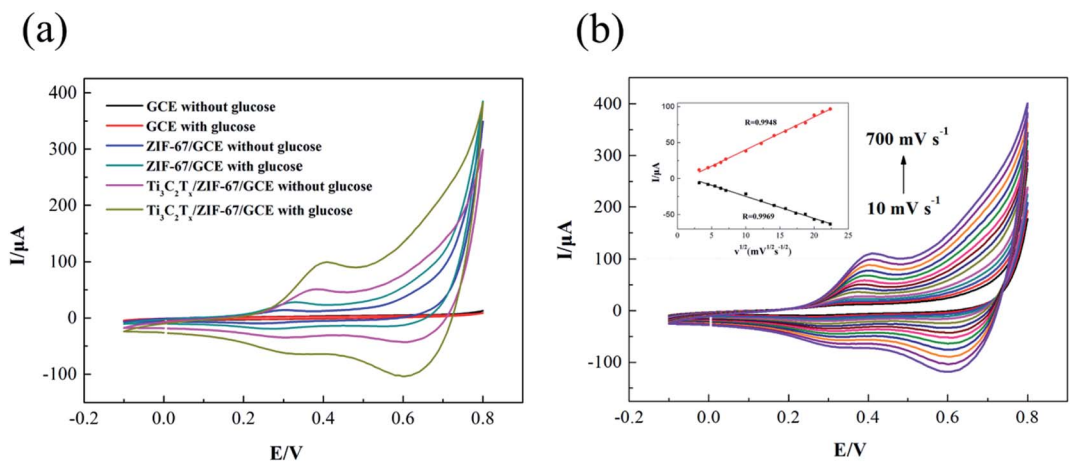

Fig. 6 (a) CVs of GCE, ZIF-67/GCE and $Ti_3C_2T_x$/GCE in the presence and absence of 1 mM glucose in 0.1 M NaOH solution at a scanning rate of 50 mV s^{-1}. (b) CVs of $Ti_3C_2T_x$/ZIF-67/GCE with different scan rate (10–500 mV s^{-1}).

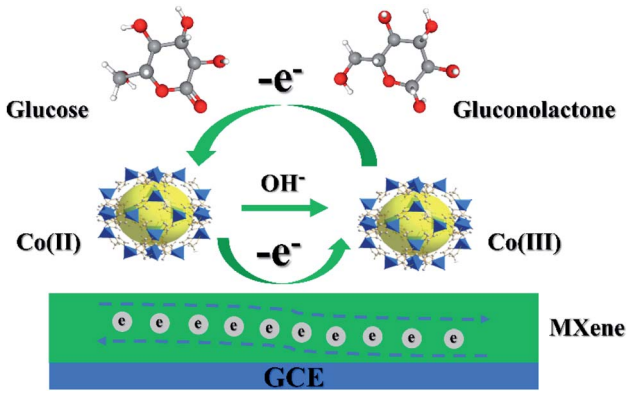

Fig. 7 The mechanism of $Ti_3C_2T_x$/ZIF-67/GCE to detect glucose in NaOH solution.

3.7 Amperometric detection of glucose on $Ti_3C_2T_x$/ZIF-67/GCE

Amperometric determination test result (Fig. 8(a)) exhibited the ampere response of $Ti_3C_2T_x$/ZIF-67/GCE towards glucose by continuously adding different amount of glucose to a stirred PBS at the fixed potential of 0.35 V. It can be seen that a quick and sensitive current response for each addition of glucose, and as the glucose concentration increasing, the response current was significantly enhanced. Fig. 8(b) presented the corresponding *I–C* calibration curve, it can be seen that the current response increased linearly over the glucose concentration ranging from 5 μmol L^{-1} to 7.5 mmol L^{-1}. The standard method (LOD = $3\sigma/q$) was used to calculate the detection limit (LOD), where σ is the standard deviation and q is the slope of the calibration graph. The LOD and linear range of $Ti_3C_2T_x$/ZIF-67/GCE was 3.81 μM and 5 μM −7.5 mM, respectively. As showed in Table 1, the $Ti_3C_2T_x$/ZIF-67 based glucose sensor had a great advantage compared with previously reported sensors, which provided an up-and-coming prospect for MOF-based glucose sensors. The excellent detection performance can be attributed to the synergetic effect of superior conductivity of $Ti_3C_2T_x$-MXene and the catalytic activity of ZIF-67. All in all, $Ti_3C_2T_x$/ZIF-67 was an effective electrode material with great potential in the trace detection of glucose.

Table 1 Comparison of performance of $Ti_3C_2T_x$/ZIF-67/GCE with those of reported sensors for glucose detection

Electrode material	Linear range (μM)	LOD (μM)	Ref.
AuNP/NG/ITO	40–16 100	12	19
Ni@Cu-MOF	5–2000	1.67	43
NiMoO4	10–8000	4.6	44
ZIF-67/GCE	5–1000	1.6	2
CoP	500–5000	9	45
Co_3O_4/NCNTs	5–2650, 4650–13 650	5	46
$Ti_3C_2T_x$/ZIF-67	5–7500	3.81	This work

3.8 Selectivity and stability of the sensor

Considering the real-time applications of the sensor, anti-interference performance has been evaluated. Fig. 9(a) showed the amperometric current response of $Ti_3C_2T_x$/ZIF-67/GCE for glucose and interference including UA (2,6,8,-trihydroxypurine), AP (Ascorbic Acid) and AA (Acetaminophen) which was often co-exist with glucose in the biological systems. It can be seen that 1 mM glucose was added at the beginning, and then a significant increase in the current response was observed. Subsequently, the same amount of AA, UA and AP were added successively, and the current response remains unchanged. To prove the selectivity of $Ti_3C_2T_x$/ZIF-67 nanocomposite, glucose was added again, and the current response was shown immediately. Actually, the $Ti_3C_2T_x$/ZIF-67 nanocomposite showed excellent selectivity and anti-interference performance for glucose sensing.

The stability of the prepared sensor was further studied by the amperometric method. As shown in Fig. 9(b), $Ti_3C_2T_x$/ZIF-67 still maintained more than 90% of the activity after 10 times of detection. The result indicated that the electrocatalytic activity of the sensor can be maintained well during the recycling

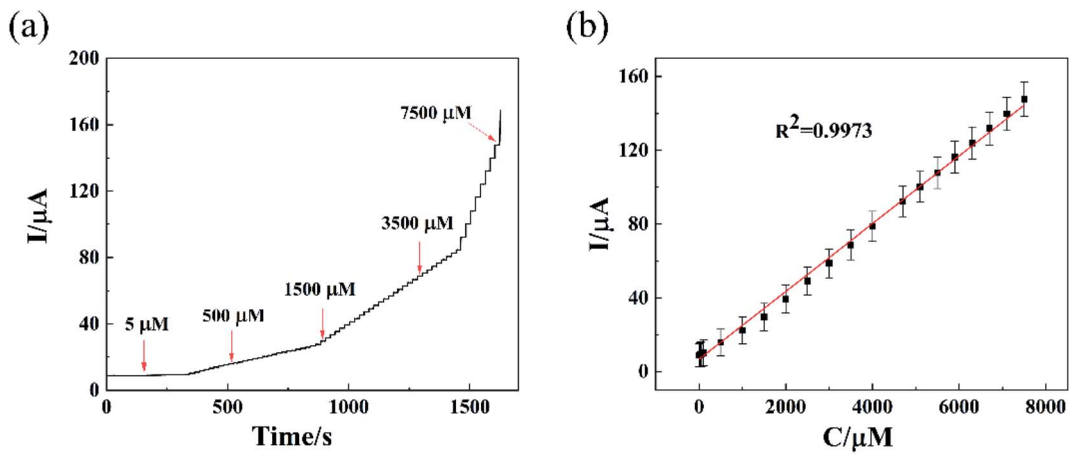

Fig. 8 (a) Typical amperometric *i–t* response on successive addition of glucose for $Ti_3C_2T_x$ in 0.1 M NaOH; (b) calibration plot of current *versus* concentration of glucose. Potential: 0.35 V.

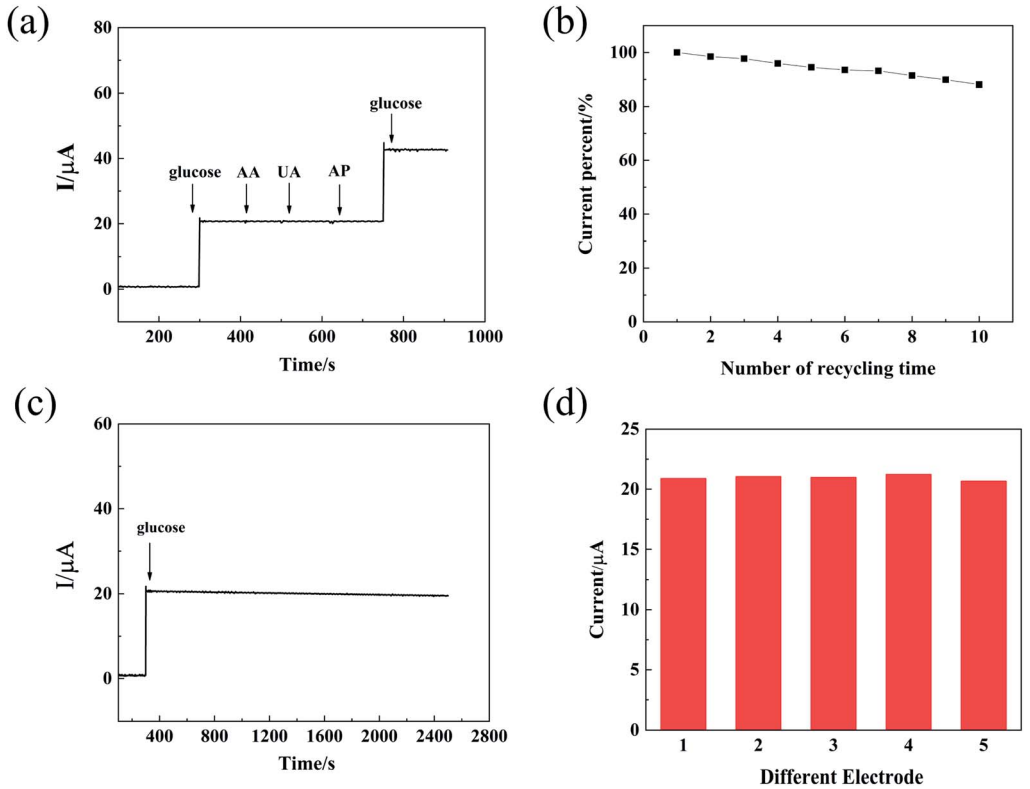

Fig. 9 (a) Amperometric *I*–*t* curve of $Ti_3C_2T_x$/ZIF-67/GCE with successive addition of 1 mM glucose and 0.5 mM AA, UA and AP in 0.1 M NaOH solution. Potential: 0.35 V; (b) change of catalytic activity of $Ti_3C_2T_x$/ZIF-67/GCE after 10 time of recycling detection in 0.1 M NaOH; (c) the amperometric *I*–*t* curve of $Ti_3C_2T_x$/ZIF-67/GCE toward 1 mM glucose over 2500 consecutive seconds; (d) reproducibility for glucose sensing with $Ti_3C_2T_x$/ZIF-67/GCE.

measurement. As shown in Fig. 9(c), the stability of the sensor was further evaluated by recording the current–time curve continuously. The current signal value kept steady within 2500 s, which showed a good stability of the sensor. Finally, the repeatability was studied by continuously testing five different $Ti_3C_2T_x$/ZIF67/GCE samples under the same conditions. As shown in the Fig. 9(d), all electrodes had similar current response and its relative standard deviation (RSD) was only 1.18%, which indicated that the sensors has an excellent repeatability.

Conclusions

In conclusion, this paper reported the preparation of ZIF-67 loaded on 2D MXene ($Ti_3C_2T_x$) nanosheets using a facile method for the first time. With the *in situ* growing ZIF-67 on 2D $Ti_3C_2T_x$, the prepared $Ti_3C_2T_x$/ZIF-67 nanocomposite combined the advantages of high electric conductivity and unique electrocatalytic activity, resulting in excellent electrocatalytic glucose oxidation performance with a wide dynamic range (5–7500 μM) and a low detection limit (3.81 μM). This work suggested that the effective combination of MOF with excellent electrocatalytic activity and 2D $Ti_3C_2T_x$ with ultra-high conductivity was a promising method for the development of high-performance electrochemical sensors.

Conflicts of interest

There are no conflicts to declare.

Acknowledgements

This study was funded by Beijing Nova Program (Z201100006820113) and National Natural Science Foundation of China (11805016).

References

1 P. Salazar, V. Rico and A. R. González-Elipe, Nickel–copper bilayer nanoporous electrode prepared by physical vapor deposition at oblique angles for the non-enzymatic determination of glucose, *Sens. Actuators, B*, 2016, **226**, 436–443.
2 W. Meng, Y. Wen, L. Dai, Z. He and L. Wang, A novel electrochemical sensor for glucose detection based on Ag@ZIF-67 nanocomposite, *Sens. Actuators, B*, 2018, **260**, 852–860.
3 R. B. Rakhi, P. Nayuk, C. Xia and H. N. Alshareef, Novel amperometric glucose biosensor based on MXene nanocomposite, *Sci. Rep.*, 2016, **6**, 1–10.
4 Y. Li, M. Xie, X. Zhang, Q. Liu, D. Lin, C. Xu, F. Xie and X. Sun, Co-MOF nanosheet array: A high-performance

electrochemical sensor for non-enzymatic glucose detection, *Sens. Actuators, B*, 2019, **278**, 126–132.

5 M. Martín, R. D. O'Neill, J. L. González-Mora and P. Salazar, The use of fluorocarbons to mitigate the oxygen dependence of glucose microbiosensors for neuroscience applications, *J. Electrochem. Soc.*, 2014, **161**, H689–H695.

6 Y. Yao, X. Han, X. Yang, J. Zhao and C. Chai, Detection of Hydrazine at MXene/ZIF-8 Nanocomposite Modified Electrode, *Chinese J. Chem.*, 2021, **39**, 330–336.

7 L. Wang, Q. Teng, X. Sun, Y. Chen, Y. Wang, H. Wang and Y. Zhang, Facile synthesis of metal-organic frameworks/ordered mesoporous carbon composites with enhanced electrocatalytic ability for hydrazine, *J. Colloid Interface Sci.*, 2018, **512**, 127–133.

8 M. Annalakshmi, P. Balasubramanian, S. M. Chen and T. W. Chen, One pot synthesis of nanospheres-like trimetallic NiFeCo nanoalloy: A superior electrocatalyst for electrochemical sensing of hydrazine in water bodies, *Sens. Actuators, B*, 2019, **296**, 126620.

9 H. Zhu, L. Li, W. Zhou, Z. Shao and X. Chen, Advances in non-enzymatic glucose sensors based on metal oxides, *J. Mater. Chem. B*, 2016, **4**, 7333–7349.

10 Y. Hu, B. Liang, L. Fang, G. Ma, G. Yang, Q. Zhu, S. Chen and X. Ye, Antifouling zwitterionic coating via electrochemically mediated atom transfer radical polymerization on enzyme-based glucose sensors for long-time stability in 37 C serum, *Langmuir*, 2016, **32**, 11763–11770.

11 S. Park, K. Cho and S. Kim, Enzyme-free glucose sensors with channels composed of necked ZnO nanoparticles on plastic, *Microelectron. Eng.*, 2011, **88**, 2611–2613.

12 A. Liu, Q. Lang, B. Liang and J. Shi, Sensitive detection of maltose and glucose based on dual enzyme-displayed bacteria electrochemical biosensor, *Biosens. Bioelectron.*, 2017, **87**, 25–30.

13 M. Baghayeri, H. Veisi and M. Ghanei-Motlagh, Amperometric glucose biosensor based on immobilization of glucose oxidase on a magnetic glassy carbon electrode modified with a novel magnetic nanocomposite, *Sens. Actuators, B*, 2017, **249**, 321–330.

14 Y. Piao, D. J. Han, M. R. Azad, M. Park and T. S. Seo, Enzyme incorporated microfluidic device for in-situ glucose detection in water-in-air microdroplets, *Biosens. Bioelectron.*, 2015, **65**, 220–225.

15 S. Badhulika, R. K. Paul, Rajesh, T. Terse and A. Mulchandani, Nonenzymatic glucose sensor based on platinum nanoflowers decorated multiwalled carbon nanotubes-graphene hybrid electrode, *Electroanalysis*, 2014, **26**, 103–108.

16 J. C. Hong and G. Qin, Preparation, Characterization and Applications of Enzyme-Free Glucose Sensors, *Key Eng. Mater.*, 2017, **730**, 172–176.

17 V. S. Subash, K. Alagumalai, S. M. Chen, R. Shanmugam and H. J. Shiuan, Ultrasonication assisted synthesis of NiO nanoparticles anchored on graphene oxide: An enzyme-free glucose sensor with ultrahigh sensitivity, *New J. Chem.*, 2020, **44**, 15071–15080.

18 B. Yang, J. Qiao, Y. Yu, L. Yuan and X. Hu, The simple-preparation of Cu–Ni/CuO–NiO using solution plasma for application in a glucose enzyme-free sensor, *New J. Chem.*, 2020, **44**, 10806–10812.

19 T. D. Thanh, J. Balamurugan, S. H. Lee, N. H. Kim and J. H. Lee, Effective seed-assisted synthesis of gold nanoparticles anchored nitrogen-doped graphene for electrochemical detection of glucose and dopamine, *Biosens. Bioelectron.*, 2016, **81**, 259–267.

20 Y. Zhao, L. Fan, B. Hong, J. Ren, M. Zhang, Q. Que and J. Ji, Nonenzymatic detection of glucose using three-dimensional PtNi nanoclusters electrodeposited on the multiwalled carbon nanotubes, *Sens. Actuators, B*, 2016, **231**, 800–810.

21 H. Zhu, L. Li, W. Zhou, Z. Shao and X. Chen, Advances in non-enzymatic glucose sensors based on metal oxides, *J. Mater. Chem. B*, 2016, **4**, 7333–7349.

22 T. Rijnaarts, R. Mejia-Ariza, R. J. M. Egberink, W. van Roosmalen and J. Huskens, Metal–Organic Frameworks (MOFs) as multivalent materials: Size control and surface functionalization by monovalent capping ligands, *Chem. - Eur. J.*, 2015, **21**, 10296–10301.

23 Q. L. Zhu and Q. Xu, Metal–organic framework composites, *Chem. Soc. Rev.*, 2014, **43**, 5468–5512.

24 R. R. Salunkhe, Y. V. Kaneti, J. Kim, J. H. Kim and Y. Yamauchi, Nanoarchitectures for metal–organic framework-derived nanoporous carbons toward supercapacitor applications, *Acc. Chem. Res.*, 2016, **49**, 2796–2806.

25 Y. Zhao, M. Seredych, J. Jagiello, Q. Zhong and T. J. Bandosz, Insight into the mechanism of CO2 adsorption on Cu–BTC and its composites with graphite oxide or aminated graphite oxide, *Chem. Eng. J.*, 2014, **239**, 399–407.

26 Y.-Z. Chen, R. Zhang, L. Jiao and H.-L. Jiang, Metal–organic framework-derived porous materials for catalysis, *Coord. Chem. Rev.*, 2018, **362**, 1–23.

27 X. Zhang, X. Wang, W. Fan and D. Sun, Pore-Environment Engineering in Multifunctional Metal-Organic Framework, *Chinese J. Chem.*, 2020, **38**, 509–524.

28 M. Sohail, M. Altaf, N. Baig, R. Jamil, M. Sher and A. Fazal, A new water stable zinc metal organic framework as an electrode material for hydrazine sensing, *New J. Chem.*, 2018, **42**, 12486–12491.

29 G. Yu, J. Xia, F. Zhang and Z. Wang, Hierarchical and hybrid RGO/ZIF-8 nanocomposite as electrochemical sensor for ultrasensitive determination of dopamine, *J. Electroanal. Chem.*, 2017, **801**, 496–502.

30 Y. Yuan, J. Xia, F. Zhang, Z. Wang and Q. Liu, Nafion/polyaniline/Zeolitic Imidazolate Framework-8 nanocomposite sensor for the electrochemical determination of dopamine, *J. Electroanal. Chem.*, 2018, **824**, 147–152.

31 D. Cheng, X. Xiao, X. Li, C. Wang, Y. Liang, Z. Yu, C. Jin, N. Zhou, M. Chen, Y. Dong, Y. Lin, Z. Xie and C. Zhang, A non-enzymatic electrochemical sensing platform based on hemin@ MOF composites for detecting hydrogen peroxide and DNA, *J. Electrochem. Soc.*, 2018, **165**, B885–B892.

32 S. Rani, B. Sharma, R. Malhotra, S. Kumar, R. S. Varma and N. Dilbaghi, Sn-MOF@ CNT nanocomposite: An efficient electrochemical sensor for detection of hydrogen peroxide, *Environ. Res.*, 2020, **191**, 110005.

33 I. A. Khan, A. Badshah, M. A. Nadeem, N. Haider and M. A. Nadeem, A copper based metal-organic framework as single source for the synthesis of electrode materials for high-performance supercapacitors and glucose sensing applications, *Int. J. Hydrogen Energy*, 2014, **39**, 19609–19620.

34 L. Shi, X. Zhu, T. Liu, H. Zhao and M. Lan, Encapsulating Cu nanoparticles into metal-organic frameworks for nonenzymatic glucose sensin, *Sens. Actuators, B*, 2016, **227**, 583–590.

35 W. Ma, Q. Jiang, P. Yu, L. Yang and L. Mao, Zeolitic imidazolate framework-based electrochemical biosensor for in vivo electrochemical measurements, *Anal. Chem.*, 2013, **85**, 7550–7557.

36 Y. Zhou, Z. Mao, W. Wang, Z. Yang and X. Liu, In-situ fabrication of graphene oxide hybrid Ni-based metal–organic framework (Ni–MOFs@ GO) with ultrahigh capacitance as electrochemical pseudocapacitor materials, *ACS Appl. Mater. Interfaces*, 2016, **8**, 28904–28916.

37 Y. Y. Zheng, C. X. Li, X. T. Ding, Q. Yang, Y. M. Qi, H. M. Zhang and L. T. Qu, Detection of dopamine at graphene-ZIF-8 nanocomposite modified electrode, *Chinese Chem. Lett.*, 2017, **28**, 1473–1478.

38 Y. Wang, C. Hou, Y. Zhang, F. He, M. Liu and X. Li, Preparation of graphene nano-sheet bonded PDA/MOF microcapsules with immobilized glucose oxidase as a mimetic multi-enzyme system for electrochemical sensing of glucos, *J. Mater. Chem. B*, 2016, **4**, 3695–3702.

39 E. Zhou, Y. Zhang, Y. Li and X. He, Cu (II)-based MOF immobilized on multiwalled carbon nanotubes: synthesis and application for nonenzymatic detection of hydrogen peroxide with high sensitivity, *Electroanalysis*, 2014, **26**, 2526–2533.

40 M. Naguib, M. Kurtoglu, V. Presser, J. Lu, J. Niu, M. Heon, L. Hultman, Y. Gogotsi and M. W. Barsoum, Two-dimensional nanocrystals produced by exfoliation of Ti3AlC2, *Adv. Mater.*, 2011, **23**, 4248–4253.

41 R. A. Soomro, S. Jawaid, Q. Zhu, Z. Abbas and B. Xu, A mini-review on MXenes as versatile substrate for advanced sensors, *Chinese Chem. Lett.*, 2020, **31**, 922–930.

42 H. Liu, C. Duan, C. Yang, W. Shen, F. Wang and Z. Zhu, A novel nitrite biosensor based on the direct electrochemistry of hemoglobin immobilized on MXene-Ti3C, *Sens. Actuators, B*, 2015, **218**, 60–66.

43 Z. Xue, L. Jia, R. R. Zhu, L. Du and Q. H. Zhao, High-performance non-enzymatic glucose electrochemical sensor constructed by transition nickel modified Ni@ Cu-MOF, *J. Electroanal. Chem.*, 2020, **858**, 113783.

44 S. H. Liao, S. Y. Lu, S. J. Bao, Y. N. Yu and M. Q. Wang, NiMoO4 nanofibres designed by electrospining technique for glucose electrocatalytic oxidation, *Anal. Chim. Acta*, 2016, **905**, 72–78.

45 Q. Q. Sun, M. Wang, S. J. Bao, Y. C. Wang and S. Gu, Analysis of cobalt phosphide (CoP) nanorods designed for non-enzyme glucose detection, *Analyst*, 2016, **141**, 256–260.

46 Y. Qin, Y. Sun, Y. Li, C. Li, L. Wang and S. Guo, MOF derived Co3O4/N-doped carbon nanotubes hybrids as efficient catalysts for sensitive detection of H2O2 and glucose, *Chinese Chem. Lett.*, 2020, **31**, 774–778.